Model-Based Iterative Reconstruction Technique for Ultralow-Dose Chest CT

Comparison of Pulmonary Nodule Detectability With the Adaptive Statistical Iterative Reconstruction Technique

Masaki Katsura, MD, Izuru Matsuda, MD, PhD, Masaaki Akahane, MD, Koichiro Yasaka, MD, Shohei Hanaoka, MD, PhD, Hiroyuki Akai, MD, PhD, Jiro Sato, MD, Akira Kunimatsu, MD, PhD, and Kuni Ohtomo, MD, PhD

Purpose: The purpose of this study was to evaluate whether model-based iterative reconstruction (MBIR) enables dose reduction over adaptive iterative reconstruction (ASIR) while maintaining diagnostic performance.

Methods: In this institutional review board–approved and Health Insurance Portability and Accountability Act–compliant study, 59 patients (mean [SD] age, 64.7 [13.4] years) gave informed consent to undergo reference-, low-, and ultralow-dose chest computed tomography (CT) with 64-row multidetector CT. The reference- and low-dose CT involved the use of automatic tube current modulation with fixed noise indices (31.5 and 70.44 at 0.625 mm, respectively) and were reconstructed with 50% ASIR-filtered back projection blending. The ultralow-dose CT was acquired with a fixed tube current-time product of 5 mA s and reconstructed with MBIR. Two radiologists evaluated 2.5- and 0.625-mm-slice–thick axial images from low-dose ASIR and ultralow-dose MBIR, recorded the pattern of each nodule candidate, and assigned each a confidence score. A reference standard was established by a consensus panel of 2 different radiologists, who identified 84 noncalcified nodules with diameters of 4 mm or greater on reference-dose ASIR (ground-glass opacity, n = 18; partly solid, n = 11; solid, n = 55). Sensitivity in nodule detection was assessed using the McNemar test. Jackknife alternative free-response receiver operating characteristic (JAFROC) analysis was applied to assess the results including confidence scores.

Results: Compared with the low-dose CT, a 78.1% decrease in dose-length product was seen with the ultralow-dose CT. No significant differences were observed between the low-dose ASIR and the ultralow-dose MBIR for overall nodule detection in sensitivity (P = 0.48–0.69) or the JAFROC analysis (P = 0.57). Likewise, no significant differences were seen for ground-glass opacity, partly solid, or solid nodule detection in sensitivity (P = 0.08–0.65) or the JAFROC analysis (P = 0.21–0.90).

Conclusions: Model-based iterative reconstruction enables nearly an 80% reduction in radiation dose for chest CT from a low-dose level to an ultralow-dose level, without affecting nodule detectability.

Key Words: model-based iterative reconstruction, adaptive statistical iterative reconstruction, radiation dose, pulmonary nodule detection

(*Invest Radiol* 2013;48: 206–212)

Lung cancer is the leading cause of death due to malignancy in most countries, with more than 1.3 million deaths estimated worldwide in 2008.[1] The disease is usually diagnosed at an advanced stage when the prognosis is poor, resulting in an overall 5-year survival rate of approximately 16%.[2] In contrast, the 5-year recurrence-free survival rate in patients with pathologically confirmed stage IA nonsmall cell lung cancer can be as high as 80%.[3,4] These data suggest that screening could help decrease mortality from lung cancer. There has been intense interest and intuitive appeal in low-dose computed tomography (CT) as a modality for lung cancer screening, and the National Lung Cancer Screening Trial (NLST), a large randomized control trial conducted in the United States, recently showed survival benefit in individuals who are at high risk for lung cancer (a 20% decrease in mortality from lung cancer) for low-dose screening CT over chest x-ray.[5]

Because of the screening nature of the examination and growing concerns about the potential harm that may derive from excess radiation, one key aim has been to keep the radiation dose delivered in previous lung cancer screening trials as low as technologically possible at the time.[6–8] The NLST involved 3 annual screenings with low-dose CT (average effective dose [ED], 1.5 mSv), resulting in a cumulative average ED of 4.5 mSv.[9] This may be acceptable among individuals who are at high risk for lung cancer, but if the feasibility of lung cancer screening CT is also to be investigated in the future for individuals who are at moderate or low risk for lung cancer, further reductions in radiation dose must be achieved while maintaining the diagnostic performance of CT for the detection of pulmonary nodules.

Several strategies have been used to enable dose reductions during CT acquisition, such as tube current modulation,[10] reduced tube voltage,[11] use of a higher pitch,[12] and noise reduction filters.[13] Use of an iterative reconstruction (IR) algorithm as an alternative to the standard filtered back projection (FBP) reconstruction algorithm is another strategy for dose reduction (see Appendix). One of the first IR algorithms released for clinical use was the adaptive statistical iterative reconstruction (ASIR) algorithm (GE Healthcare, Waukesha, WI). Adaptive statistical iterative reconstruction algorithm significantly reduces image noise compared with the FBP algorithm (see Appendix), provides dose-reduced clinical images with preserved diagnostic value,[14–24] and has been widely used for dose reduction in many CT systems. The recently developed model-based iterative reconstruction (MBIR) is a much more complex and advanced algorithm than ASIR is: it provides significant reductions in image noise and streak artifacts, significantly improves spatial resolution, and has the potential to allow further reductions in radiation dose without compromising image quality (see Appendix).[25,26] On the other hand, MBIR is also known for some unique imaging features, such as a pixelated blotchy appearance,[27,28] and the impact of these features on lesion detectability remains unclear. Up to this point, few studies have assessed the ability of MBIR to detect and localize lesions.[28,29] The purpose of this study was thus to evaluate whether MBIR enables further reductions in

Received for publication September 30, 2012; and accepted for publication, after revision, November 18, 2012.
From the Department of Radiology, Graduate School of Medicine, The University of Tokyo, Tokyo, Japan.
Presented at the 98th Scientific Assembly and Annual Meeting of Radiological Society of North America.
Conflicts of interest and sources of funding: none declared.
Reprints: Masaki Katsura, MD, Department of Radiology, Graduate School of Medicine, The University of Tokyo, 7-3-1 Hongo, Bunkyo-ku, Tokyo 113-8655, Japan. E-mail: mkatsura-tky@umin.ac.jp.

ISSN: 0020-9996/13/4804–0206

TABLE 1. Patient Characteristics and CT Parameters

Sex, men/women	32/27
Age, y	64.7 (13.4)
Body weight, kg	59.0 (14.1)
Acquisition mode	Helical
Tube voltage, kV(p)	120
Field of view, mm	350*
Gantry rotation time, s	0.5
Table speed, mm per gantry rotation	39.37
Detector configuration, mm	64 × 0.625
Reconstructed section thickness, mm	0.625
Pitch	0.984:1

Data represent mean (SD) for each value, unless indicated otherwise.

The main clinical indications for chest CT were as follows: follow-up for a pulmonary nodule (n = 15), abnormal results of chest radiography (n = 10), interstitial lung disease (n = 10), staging or restaging of known or suspected malignancy (n = 10), GGO (n = 3), obstructive pulmonary disease (n = 3), hemoptysis (n = 3), mediastinal mass (n = 2), sarcoidosis (n = 1), pulmonary tuberculosis (n = 1), and asbestosis (n = 1).

*Field of view was typically set at 350 mm, but it was adjusted according to patient size.

radiation dose over ASIR while maintaining diagnostic performance for the detection of pulmonary nodules.

MATERIALS AND METHODS

This prospective clinical study was compliant with the Health Insurance Portability and Accountability Act guidelines and was approved by the Human Research Committee at our institution.

Patients

The Radiology Information System was checked to identify patients scheduled for unenhanced standard-of-care clinical chest CT examinations at a single tertiary care center. Inclusion criteria for the present study were as follows: age of older than 18 years, patient scheduled for unenhanced standard-of-care CT examination of the chest, the ability to provide written informed consent, and the ability to hold his/her breath and remain still for at least 10 seconds. Patients who were unable to provide written informed consent, follow verbal commands for breath-holding, or remain still for the duration of CT acquisition were excluded. Women who were pregnant or were trying to get pregnant were also excluded. Each potential participant was given a detailed informed consent form that was written in simple language about the objectives, methods, and risks of study participation. The study procedure, which involved acquisition of a reference-dose CT followed by low- and ultralow-dose CT (both discussed later in detail), was explained to the participants. The participants were also informed that the total radiation exposure from the reference-, low-, and ultralow-dose CT acquisitions would not exceed the radiation dose for the standard-of-care chest CT in our institution. The risks associated with study participation, particularly the possible influence on diagnostic performance, in which the reference dose in the present study was expected to be slightly lower compared with the radiation doses for the standard-of-care CT, were explained to the participants in simple language. The participants were also informed that they would not receive any remuneration or benefit from their participation in the study.

Between July 1, 2011, and July 28, 2011, a total of 113 consecutive eligible patients were prospectively identified. Nine patients declined to participate in the study, and 104 provided informed consent. After the CT acquisition, images were reviewed by the main author (M.K., with 4 years of imaging experience) and 30 patients who were associated with the following conditions that may hinder the interpretation of studies for pulmonary nodules were excluded: severe lung structural distortions (including the postoperative state), more than 10 nodules within 1 lobe (eg, nontuberculosis mycobacterial disease), numerous nodules throughout the lungs (eg, numerous lung metastases), or consolidation involving more than 1 segment. From the remaining 74 patients, images from 15 patients were selected using a random number table, which was used for training purposes (to understand the evaluation system) by 2 thoracic radiologists (K.Y. and S.H., with 3 and 10 years of experience, respectively), and subsequently eliminated from the remaining analyses. As a result, 59 patients were included in the final analysis. Demographic information for each patient is presented in Table 1.

Computed Tomographic Data Acquisition

Unenhanced chest CT as the reference-dose CT followed by low- and ultralow-dose CT was performed using a 64-row multidetector CT system (Discovery CT750 HD; GE Healthcare, Waukesha, WI). All patients in the present study were able to undergo chest CT in the supine position with both arms elevated, with a single breath-hold for each acquisition. Imaging parameters for the reference-, low-, and ultralow-dose CT were held constant with the exception of radiation dose, as summarized in Table 1. To minimize positional differences between the 3 acquisitions, the time between each scan was kept to a minimum (about 10 seconds or less). To avoid contrast enhancement bias due to delays in imaging from the start of contrast injection, only the unenhanced CT images were included in the present study. The CHEST kernel (a proprietary kernel of GE Healthcare, Waukesha, WI) was used

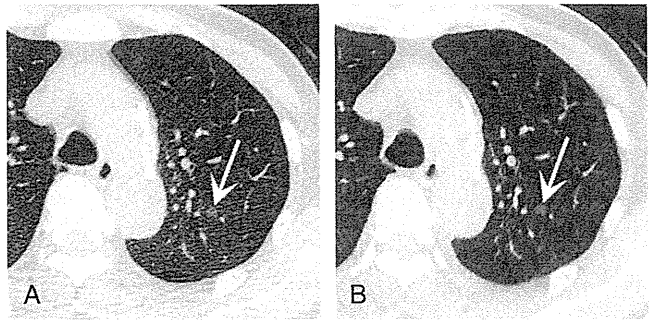

FIGURE 1. Imaging results of a 79-year-old man (weight, 64 kg): A, Low-dose CT (DLP, 64.2 mGy-cm) reconstructed with ASIR. B, Ultralow-dose CT (DLP, 15.4 mGy-cm) reconstructed with MBIR. The prominent streak artifact from the shoulders on the low-dose ASIR (A) interferes with the adequate visualization of the GGO nodule in the left upper lobe (arrow), which was missed by both radiologists. In the ultralow-dose MBIR (B), the nodule is clearly depicted (arrow) and was identified by both radiologists. The images are shown in lung window settings (WW, 1,500 HU; WL, −600 HU).

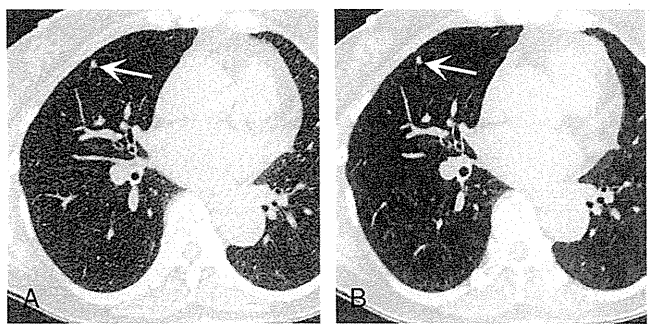

FIGURE 2. Imaging results of a 64-year-old woman (weight, 52 kg): A, Low-dose CT (DLP, 36.4 mGy-cm) reconstructed with ASIR. B, Ultralow-dose CT (DLP, 14.0 mGy-cm) reconstructed with MBIR. Both images provide adequate visualization of the solid nodule in the right middle lobe (arrows), which was identified by both radiologists.

for image reconstruction. This kernel is equivalent to the LUNG kernel (a proprietary kernel of GE Healthcare, Waukesha, WI) for depiction of the lung and equivalent to the SOFT-TISSUE kernel (a proprietary kernel of GE Healthcare, Waukesha, WI) for depiction of mediastinal soft-tissue structures.[30,31] All images were reconstructed with 0.625-mm–thick axial slices, and the images with increased slice thickness of 2.5 mm (by averaging) were also used for interpretation as necessary, in accordance with the NLST protocol.[5] The images with coronal/sagittal reformats were not used for evaluation in this study because the preliminary results of our phantom experiments indicated that MBIR and ASIR behave differently in image noise when reformatted into coronal and sagittal slices (I. Matsuda, unpublished data, November 2012).

Radiation Dose Setting

Both reference- and low-dose CT protocols involved the use of automatic tube current modulation (Auto mA 3D; GE Healthcare). The operator-selected noise index (NI) level modulates the tube current during gantry rotation to achieve a predicted average statistical noise level in the images of the reconstruction slice thickness specified. In the present study, a fixed NI of 31.5 at 0.625 mm was used for the reference-dose CT, which, theoretically, should achieve the same radiation dose for the reference-dose chest CT described in the radiology literature.[14,32] As for the low-dose CT (NI of 70.44 at 0.625 mm), we referred to the mean ED for the low-dose CT described in the NLST (1.5 mSv),[9] which is about one-fifth of the radiation dose for the reference-dose chest CT described in the radiology literature.[14,32] The ultralow-dose CT was acquired using a fixed tube current-time product of 5 mA s.

Image Reconstruction

The images for the reference- and low-dose CT were reconstructed with blending of 50% FBP and 50% ASIR image data (ASIR50). The blending factor of 50% was chosen on the basis of the literature[16,17] and the recommendations of the vendor. The images for the ultralow-dose CT were reconstructed with MBIR. Blending with FBP does not apply to MBIR because this is a pure IR technique (see Appendix). Thus, 3 axial image data sets (reference-dose ASIR, low-dose ASIR, and ultralow-dose MBIR) were generated for each patient. The low-dose ASIR and the ultralow-dose MBIR were used for image interpretation (Figs. 1 and 2), after removing patient information to allow blinded evaluation. The reference-dose ASIR was used for establishing a reference standard.

Image Interpretation

Two thoracic radiologists (K.Y. and S.H.) independently evaluated the ultralow-dose MBIR images from the 59 patients (ultralow-dose MBIR session), then evaluated the low-dose ASIR images (low-dose ASIR session), using a commercial software (EV Insite; PSP Corporation, Tokyo, Japan). The image interpretation was performed using both 2.5- and 0.625-mm–thick axial images as necessary, in accordance with the NLST protocol.[5] The images in each reading session were presented in random order to each reader. To minimize recall bias, the 2 reading sessions were separated by 4 weeks. Both radiologists already had 3 years of experience with ASIR images at the time of the present study because of its introduction into our department in January 2009. They had little experience with MBIR images at the time of the study, although they became familiar with MBIR images through the training session. The radiologists, who were blinded to patient data and clinical information, were instructed with the following: to identify all noncalcified pulmonary nodules with long-axis diameters of 4 mm or greater using a procedure similar to that used in routine clinical practice, using a caliper on the monitor; to report the location and radiologic pattern (ground-glass opacity [GGO], partly solid, or solid) of each candidate nodule, and to assign a confidence level for each nodule using a 4-point scale (1, nodule probably not present; 2, nodule presence equivocal; 3, nodule probably present; 4, nodule definitely present), according to the free-response receiver operating characteristics (FROC) paradigm. For each session, the radiologists were given an unlimited amount of time to independently analyze the images. In addition to the default preselected lung window settings (window width [WW], 1500 Hounsfield units [HU]; window level [WL], −600 HU), the radiologists were allowed to change the WW and WL for ease of assessment.

Some of the images used for evaluating pulmonary nodule detection in this study were also used for assessing image quality characteristics in a previous study.[28] The previous study was conducted merely for image quality assessment and is completely different from the present study in nature. The present study specifically focused on diagnostic performance for the detection of pulmonary nodules by 2 different thoracic radiologists, neither of whom were involved in the image interpretation process for the previous study.

Reference Standard

A consensus panel of 2 different radiologists (I.M. and H.A., with 6 and 8 years of experience, respectively) independently interpreted the entire set of images from the reference-dose ASIR and identified noncalcified pulmonary nodules with diameters of 4 mm or greater, in accordance with the positive findings in the NLST.[5] Interpretation of images for establishment of the reference standard occurred both as a free search through the CT sections and as a directed analysis of all candidate nodules originally identified by the previous 2 radiologists (K.Y. and S.H.). The panel members (I.M. and H.A.), without knowledge of the source of detection of the candidate nodules, assessed each candidate and arrived at a final consensus decision as to whether the finding represented a nodule (true-positive finding) or not (false-positive finding). In addition, the long-axis diameter of each

nodule (true-positive detection) was measured by a different radiologist (M.K.) using digital calipers.

Radiation Dose Evaluation

To evaluate the radiation dose, the estimated CT dose index volume (CTDIvol) and dose-length product (DLP) were recorded for each image data set after the completion of the CT examination, according to the dose report. Effective doses were estimated from DLP using a constant of 0.014 mSv/mGy-cm, as reported in the literature for chest CT.[33]

Statistical Analyses

The results of each radiologist in the ultralow-dose MBIR and the low-dose ASIR were compared with the reference standard, and the sensitivity in detecting pulmonary nodules was assessed. The statistical significance of any difference between the ultralow-dose MBIR and the low-dose ASIR for each radiologist was assessed using the McNemar test. The data were analyzed using JMP 9.0.0 software (SAS Institute, Cary, NC). The results, including confidence levels, were used to generate jackknife alternative free-response receiver operating characteristic (JAFROC) plots. The JAFROC analysis[34,35] was used for the evaluation of radiologist performance in the detection of pulmonary nodules in the ultralow-dose MBIR and the low-dose ASIR. The JAFROC analysis has been proposed for estimating the statistical significance of differences between modalities when location issues are relevant and has been widely used in multiple previous studies in the radiology literature.[36–39] The JAFROC analysis is based on a FROC paradigm and accounts for reader variation.[34,35,40] Conventional ROC analysis is of limited value for this kind of application because only 1 response per image can be used per case, and the location of the response cannot be taken into account in the evaluation. In contrast, the FROC analysis allows evaluation of the performance of radiologists in diagnosing medical images using multiple responses, each with information on the confidence level and location. For statistical testing of differences in radiologist performance between the ultralow-dose MBIR and the low-dose ASIR, JAFROC version 4.0 software (http://www.devchakraborty.com) was applied to estimate figure-of-merit (FOM) values (*analog of the area under the ROC curve*, defined as the probability that a true-positive confidence rating exceeds any false-positive rating on cases without nodules) of each modality (the ultralow-dose MBIR and the low-dose ASIR) with 95% confidence intervals. An F test was used internally for the analysis of variance, yielding a P value for rejecting the null hypothesis of no difference between the 2 modalities. A value of $P < 0.05$ was considered statistically significant.

RESULTS

Radiation Dose

Radiation dose descriptors acquired with the reference-, low-, and ultralow-dose CT for the 59 patients are summarized in Table 2. Compared with the low-dose CT, a 78.1% decrease in DLP was seen with the ultralow-dose CT.

TABLE 2. Comparison of Radiation Dose for the Reference-, Low-, and Ultralow-Dose CT

	Reference-Dose	Low-Dose	Ultralow-Dose
CTDIvol, mGy	8.29 (4.60)	1.77 (1.29)	0.39 (0.00)
DLP, mGy-cm	307.7 (178.1)	66.0 (50.8)	14.5 (1.1)
ED, mSv	4.31	0.92	0.20

Data represent mean (SD) for each value.

Compared with the low-dose CT, a 78.0% decrease in CTDIvol and a 78.1% decrease in DLP were seen with the ultralow-dose CT.

TABLE 3. Number and Size of Nodules

Pattern of Nodule	Number	Size, mm
GGO	18	8.0 (4.4)
Partly solid	11	11.3 (6.4)
Solid	55	7.0 (4.6)

Data represent mean (SD) for each value.

Results of Nodule Detection

The consensus panel found 84 noncalcified nodules of 4 mm in diameter or more on the reference-dose ASIR (GGO, n = 18; partly solid, n = 11; solid, n = 55) in the 59 patients. No nodules were found in 18 patients. The mean diameter of each nodule according to the 3 radiological patterns is shown in Table 3.

Sensitivity data for the detection of overall nodules and according to the 3 radiological patterns are shown in Table 4. No significant differences were identified between the low-dose ASIR and the ultralow-dose MBIR of both radiologists for the overall nodule detection (61%–67%; $P = 0.48$–0.69). Similarly, no significant differences were observed for GGO, partly solid, or solid nodule detection (50%–91%; $P = 0.08$–0.65).

Jackknife Alternative Free-Response Receiver Operating Characteristic Analysis

Figure-of-merit values for the 2 radiologists in the detection of all pulmonary nodules are summarized in Table 5. In the overall nodules, no significant differences were identified between the low-dose ASIR and the ultralow-dose MBIR in the FOM values ($P = 0.57$). The JAFROC analysis also revealed no significant differences between the low-dose ASIR and the ultralow-dose MBIR for GGO, partly solid, or solid nodule detection ($P = 0.21$–0.90).

DISCUSSION

In the present study, nodule detectability in the low-dose chest CT reconstructed with ASIR and the ultralow-dose CT reconstructed with MBIR were directly compared in the same patients. Diagnostic performance for nodule detection in the MBIR images acquired with nearly 80% dose reduction (ultralow-dose) did not differ significantly from that in the low-dose ASIR (representing the dose for lung cancer screening CT), irrespective of the characteristics of the nodules as GGO, partly solid, or solid. To the best of our knowledge, this is the first clinical study to evaluate the ability of MBIR to allow further radiation dose reduction over ASIR by directly comparing the diagnostic performance for the detection of pulmonary nodules in the same patients.

As radiation dose decreases by 1/x, the image noise is known to increase by the square root of x in FBP and subsequently in hybrid IR algorithms that involve blending with FBP such as ASIR, which renders the visualization of nodules in dose-reduced chest CT. However, our preliminary results from phantom experiments indicated that MBIR, a pure IR algorithm, behaves differently: as radiation dose decreases by 1/x, image noise increases only by the fourth root of x (unpublished data), resulting in a relatively lower increase in noise compared with FBP or hybrid IR-reconstructed images. Moreover, MBIR also provides significant reductions in streak artifacts and significant improvements in spatial resolution.[25,26] The ultralow-dose MBIR in the present study showed no significant differences in the overall nodule detection from the low-dose ASIR in sensitivity for both radiologists. Our sensitivity data (50%–91%) are similar to those in a previous study that assessed pulmonary nodule detection in standard-dose CT.[39] The JAFROC analysis also revealed no significant differences between the low-dose ASIR and the ultralow-dose MBIR, irrespective of nodule characteristics as GGO, partly solid, or solid

TABLE 4. Sensitivity Data for Nodule Detection

	Radiologist 1			Radiologist 2		
Pattern of Nodule	**Ultralow MBIR**	**Low ASIR**	***P***	**Ultralow MBIR**	**Low ASIR**	***P***
Overall (n = 84)	56/84 (67)	54/84 (64)	0.69	55/84 (65)	51/84 (61)	0.48
GGO (n = 18)	12/18 (67)	9/18 (50)	0.08	9/18 (50)	11/18 (61)	0.41
Partly solid (n = 11)	10/11 (91)	7/11 (64)	0.08	7/11 (64)	6/11 (55)	0.65
Solid (n = 55)	34/55 (62)	38/55 (69)	0.37	39/55 (71)	34/55 (62)	0.28

No significant differences were seen between the low-dose ASIR and the ultralow-dose MBIR for both radiologists for the overall nodule, GGO, partly solid, or solid nodule detection (McNemar test).

nodules. A pixelated blotchy appearance was noted in almost all ultralow-dose MBIR images but did not seem to affect the diagnostic performance of the radiologists, neither of whom had little experience with MBIR images before the present study. Recently, Yamada et al[41] compared the diagnostic performance of "ultralow-dose" MBIR (ED, 0.17 mSv) and "ultralow-dose" FBP for pulmonary nodule detection, using "low-dose" FBP (ED, 2.10 mSv) as the reference standard. The present study differs from their study in that we used reference-dose ASIR to establish a more robust reference standard, and moreover, we directly compared the diagnostic performance of the ultralow-dose MBIR and the low-dose ASIR to evaluate whether MBIR enables further radiation dose reduction over ASIR. The present results indicate the substantial potential of MBIR for achieving further radiation dose reductions without affecting nodule detectability, irrespective of nodule characteristics. The results also indicate that ultralow-dose CT may become feasible with the use of a pure IR algorithm such as MBIR.

Many studies have examined the use of low-dose chest CT for lung cancer screening.[6–9,42–45] The radiation dose delivered by lung screening CT has been aimed to be as low as technologically possible, typically ranging from 0.6 to 1.5 mSv in previous lung cancer screening CT trials.[7–9] The ED for the low-dose CT in the present study turned out to be lower than the average ED is for the low-dose CT described in the NLST (1.5 mSv),[9] most likely because of the small body size of the patients. The ultralow-dose CT was acquired with a nearly 80% reduction in dose compared with the low-dose CT. The present results indicate that lung cancer screening CT may be lowered even to ultralow-dose levels using pure IR algorithms such as MBIR. We acknowledge that the patients in the present study do not necessarily reflect the target population for lung cancer screening in terms of clinical and social characteristics, prevalence of lesions, or background lung conditions. However, our results strongly support the potential of ultralow-dose MBIR for the purpose of lung cancer screening. Longitudinal studies with an increased number of participants (the sample size should be determined by statistical power analysis) in a targeted population specifically aimed at assessing lung cancer mortality are necessary. Ultralow-dose MBIR should also be assessed in future studies for other screening purposes, such as CT colonography. In addition, MBIR may be considered for patients who require substantial dose reduction, such as infants and young patients, and those with radiosensitive genetic disorders such as ataxia telangiectasia. Because the impact of MBIR on lesion detectability may differ between body regions and for different lesion characteristics (eg, size, attenuation, contrast), MBIR should be evaluated according to the purpose of each examination in future studies.

Several limitations of this study must be considered. First, the body size of patients in this study was generally small. Our results of the ultralow-dose CT acquired using a fixed tube current-time product of 5 mA s may not necessarily apply to patients who are extremely large or obese. This needs to be investigated in future studies using automatic tube current modulation with appropriate NI settings. Second, all chest CT examinations were performed without intravenous administration of contrast medium. The contrast enhancement effect itself has not yet been thoroughly assessed in MBIR, and the presence of streak artifacts from the superior vena cava is another important issue that needs to be considered in contrast-enhanced chest CT. These are not issues in lung cancer screening CT, which does not usually involve the use of contrast medium, but these issues should be investigated in future studies to further assess the feasibility of MBIR for clinical use. A third limitation of the study is that the results may not be applicable to similar iterative reconstruction methods available from other vendors.

In conclusion, MBIR enables a nearly 80% reduction in radiation dose for chest CT from a low-dose level to an ultralow-dose level, without affecting nodule detectability. Ultralow-dose CT is expected to become feasible for lung cancer screening with the use of pure IR algorithms such as MBIR.

TABLE 5. Figure-of-Merit Values Obtained From the JAFROC Analysis

	FOM Values (95% Confidence Interval)		
Pattern of Nodule	**Ultralow MBIR**	**Low ASIR**	***P***
Overall (n = 84)	0.817 (0.776–0.859)	0.802 (0.746–0.857)	0.57
GGO (n = 18)	0.793 (0.708–0.879)	0.750 (0.654–0.846)	0.22
Partly solid (n = 11)	0.885 (0.511–1.260)	0.794 (0.659–0.928)	0.21
Solid (n = 55)	0.832 (0.735–0.929)	0.827 (0.742–0.913)	0.90

No significant differences in JAFROC FOM values were identified between the low-dose ASIR and the ultralow-dose MBIR for the overall nodule, GGO, partly solid, or solid nodule detection.

ACKNOWLEDGMENTS

The authors thank Kosuke Sasaki, MS, and Koji Segawa, RT, for their technical support and assistance in data acquisition.

REFERENCES

1. Ferlay J, Shin H, Bray F, et al. Estimates of worldwide burden of cancer in 2008: GLOBOCAN 2008. *Int J Cancer*. 2010;127:2893–2917.
2. Cancer Facts & Figures 2012. American Cancer Society Web site. http://www.cancer.org/Research/CancerFactsFigures/CancerFactsFigures/cancer-facts-figures-2012. Accessed 30 September 2012.
3. Cerfolio RJ, Bryant AS. Survival of patients with true pathologic stage I non-small cell lung cancer. *Ann Thorac Surg*. 2009;88:917–923.
4. Carr SR, Schuchert MJ, Pennathur A, et al. Impact of tumor size on outcomes after anatomic lung resection for stage 1A non-small cell lung cancer based on the current staging system. *J Thorac Cardiovasc Surg*. 2012;143:390–397.
5. National Lung Screening Trial Research Team, Aberle DR, Adams AM, et al. Reduced lung-cancer mortality with low-dose computed tomographic screening. *N Engl J Med*. 2011;365:395–409.
6. Henschke CI, McCauley DI, Yankelevitz DF, et al. Early lung cancer action project: a summary of the findings on baseline screening. *Oncologist*. 2001; 6:147–152.

7. Swensen SJ, Jett JR, Hartman TE, et al. Lung cancer screening with CT: Mayo Clinic experience. *Radiology.* 2003;226:756–761.
8. Diederich S, Thomas M, Semik M, et al. Screening for early lung cancer with low-dose spiral computed tomography: results of annual follow-up examinations in asymptomatic smokers. *Eur Radiol.* 2004;14:691–702.
9. National Lung Screening Trial Research Team, Aberle DR, Berg CD, et al. The National Lung Screening Trial: overview and study design. *Radiology.* 2011;258:243–253.
10. Kalra MK, Maher MM, Toth TL, et al. Strategies for CT radiation dose optimization. *Radiology.* 2004;230:619–628.
11. Heyer CM, Mohr PS, Lemburg SP, et al. Image quality and radiation exposure at pulmonary CT angiography with 100- or 120-kVp protocol: prospective randomized study. *Radiology.* 2007;245:577–583.
12. Baumueller S, Alkadhi H, Stolzmann P, et al. Computed tomography of the lung in the high-pitch mode: is breath holding still required? *Invest Radiol.* 2011;46:240–245.
13. Kalra MK, Maher MM, Sahani DV, et al. Low-dose CT of the abdomen: evaluation of image improvement with use of noise reduction filters pilot study. *Radiology.* 2003;228:251–256.
14. Prakash P, Kalra MK, Digumarthy SR, et al. Radiation dose reduction with chest computed tomography using adaptive statistical iterative reconstruction technique: initial experience. *J Comput Assist Tomogr.* 2010;34:40–45.
15. Leipsic J, Labounty TM, Heilbron B, et al. Adaptive statistical iterative reconstruction: assessment of image noise and image quality in coronary CT angiography. *AJR Am J Roentgenol.* 2010;195:649–654.
16. Singh S, Kalra MK, Hsieh J, et al. Abdominal CT: comparison of adaptive statistical iterative and filtered back projection reconstruction techniques. *Radiology.* 2010;257:373–383.
17. Prakash P, Kalra MK, Kambadakone AK, et al. Reducing abdominal CT radiation dose with adaptive statistical iterative reconstruction technique. *Invest Radiol.* 2010;45:202–210.
18. Singh S, Kalra MK, Gilman MD, et al. Adaptive statistical iterative reconstruction technique for radiation dose reduction in chest CT: a pilot study. *Radiology.* 2011;259:565–573.
19. Kilic K, Erbas G, Guryildirim M, et al. Lowering the dose in head CT using adaptive statistical iterative reconstruction. *AJNR Am J Neuroradiol.* 2011; 32:1578–1582.
20. Mieville FA, Gudinchet F, Rizzo E, et al. Paediatric cardiac CT examinations: impact of the iterative reconstruction method ASIR on image quality—preliminary findings. *Pediatr Radiol.* 2011;41:1154–1164.
21. Singh S, Kalra MK, Shenoy-Bhangle AS, et al. Radiation dose reduction with hybrid iterative reconstruction for pediatric CT. *Radiology.* 2012;263:537–546.
22. Craig O, O'Neill S, O'Neill F, et al. Diagnostic accuracy of computed tomography using lower doses of radiation for patients with Crohn's disease. *Clin Gastroenterol Hepatol.* 2012;10:886–892.
23. Desai GS, Uppot RN, Yu EW, et al. Impact of iterative reconstruction on image quality and radiation dose in multidetector CT of large body size adults. *Eur Radiol.* 2012;22:1631–1640.
24. Kaza RK, Platt JF, Al-Hawary MM, et al. CT enterography at 80 kVp with adaptive statistical iterative reconstruction versus at 120 kVp with standard reconstruction: image quality, diagnostic adequacy, and dose reduction. *AJR Am J Roentgenol.* 2012;198:1084–1092.
25. Thibault JB, Sauer KD, Bouman CA, et al. A three-dimensional statistical approach to improved image quality for multislice helical CT. *Med Phys.* 2007;34:4526–4544.
26. Yu Z, Thibault JB, Bouman CA, et al. Fast model-based x-ray CT reconstruction using spatially nonhomogeneous ICD optimization. *IEEE Trans Image Process.* 2011;20:161–175.
27. Nelson RC, Feuerlein S, Boll DT. New iterative reconstruction techniques for cardiovascular computed tomography: how do they work, and what are the advantages and disadvantages? *J Cardiovasc Comput Tomogr.* 2011;5:286–292.
28. Katsura M, Matsuda I, Akahane M, et al. Model-based iterative reconstruction technique for radiation dose reduction in chest CT: comparison with the adaptive statistical iterative reconstruction technique. *Eur Radiol.* 2012;22:1613–1623.
29. Singh S, Kalra MK, Do S, et al. Comparison of hybrid and pure iterative reconstruction techniques with conventional filtered back projection: dose reduction potential in the abdomen. *J Comput Assist Tomogr.* 2012;36:347–353.
30. Strub WM, Weiss KL, Sun D. Hybrid reconstruction kernel: optimized chest CT. *AJR Am J Roentgenol.* 2007;189:W115–W116.
31. Weiss KL, Cornelius RS, Greeley AL, et al. Hybrid convolution kernel: optimized CT of the head, neck, and spine. *AJR Am J Roentgenol.* 2011;196:403–406.
32. Prakash P, Kalra MK, Ackman JB, et al. Diffuse lung disease: CT of the chest with adaptive statistical iterative reconstruction technique. *Radiology.* 2010; 256:261–269.
33. American Association of Physicists in Medicine. The measurement, reporting, and management of radiation dose in CT; January 2008. Available at: http://www.aapm.org/pubs/reports/rpt_96.pdf. Accessed September 30, 2012.
34. Chakraborty DP, Berbaum KS. Observer studies involving detection and localization: modeling, analysis, and validation. *Med Phys.* 2004;31:2313–2330.
35. Chakraborty DP. Analysis of location specific observer performance data: validated extensions of the jackknife free-response (JAFROC) method. *Acad Radiol.* 2006;13:1187–1193.
36. Vikgren J, Zachrisson S, Svalkvist A, et al. Comparison of chest tomosynthesis and chest radiography for detection of pulmonary nodules: human observer study of clinical cases. *Radiology.* 2008;249:1034–1041.
37. Hirose T, Nitta N, Shiraishi J, et al. Evaluation of computer-aided diagnosis (CAD) software for the detection of lung nodules on multidetector row computed tomography (MDCT): JAFROC study for the improvement in radiologists' diagnostic accuracy. *Acad Radiol.* 2008;15:1505–1512.
38. Zachrisson S, Vikgren J, Svalkvist A, et al. Effect of clinical experience of chest tomosynthesis on detection of pulmonary nodules. *Acta Radiol.* 2009;50:884–891.
39. Yanagawa M, Honda O, Yoshida S, et al. Commercially available computer-aided detection system for pulmonary nodules on thin-section images using 64 detectors-row CT: preliminary study of 48 cases. *Acad Radiol.* 2009;16:924–933.
40. Chakraborty DP. Maximum likelihood analysis of free-response receiver operating characteristic (FROC) data. *Med Phys.* 1989;16:561–568.
41. Yamada Y, Jinzaki M, Tanami Y, et al. Model-based iterative reconstruction technique for ultralow-dose computed tomography of the lung: a pilot study. *Invest Radiol.* 2012;47:482–489.
42. Sone S, Li F, Yang ZG, et al. Results of three-year mass screening programme for lung cancer using mobile low-dose spiral computed tomography scanner. *Br J Cancer.* 2001;84:25–32.
43. Nawa T, Nakagawa T, Kusano S, et al. Lung cancer screening using low-dose spiral CT: results of baseline and 1-year follow-up studies. *Chest.* 2002; 122:15–20.
44. Sobue T, Moriyama N, Kaneko M, et al. Screening for lung cancer with low-dose helical computed tomography: anti-lung cancer association project. *J Clin Oncol.* 2002;20:911–920.
45. Gohagan JK, Marcus PM, Fagerstrom RM, et al. Final results of the Lung Screening Study, a randomized feasibility study of spiral CT versus chest x-ray screening for lung cancer. *Lung Cancer.* 2005;47:9–15.

APPENDIX

Adaptive iterative reconstruction and MBIR are new IR algorithms. Unlike the conventional FBP, which is based on simpler mathematical assumptions of the tomographic imaging system, IR generates a set of synthesized projections by accurately modeling the data collection process in CT. The model incorporates statistical system information (including photon statistics and electronic noise in the data acquisition system) and details of the system optics (including the size of each detector cell, dimensions of the focal spot, and the shape and size of each image voxel). The synthesized image is mathematically compared and corrected with the actual measurement to adjust estimation of the object's image. The technique then iterates this comparison and correction step to achieve close proximity between actual and measured projections. Inconsistencies in the projection measurement due to limited photon statistics and electronic noise are corrected with multiple iterations. These data-processing steps help to improve image quality from the noise and resolution perspectives but prolong the reconstruction duration compared with FBP because of the intensive computations particularly required for incorporating system optics information.

The ASIR technique models just the photons and electronic noise statistics that primarily affect image noise, which are not computationally intensive or time-consuming. This enables near real-time display of images at the time of imaging. Adaptive iterative reconstruction also differs from other IR techniques in that the vendor provides a blending tool to blend the FBP with the ASIR images ("hybrid IR"). This is accomplished by reconstruction of CT raw data with both FBP and ASIR techniques and then performing a weighted summation of each data set for the final reconstructed images. Prior studies have already shown that ASIR provides low-dose clinical images with a reduction in image noise compared with the FBP algorithm and preserved diagnostic value.[14–24]

The MBIR technique, on the other hand, is a pure IR technique that does not involve blending with FBP images and is mathematically more complex and accurate than ASIR is. Model-based iterative reconstruction not only incorporates modeling of photon and noise statistics such as ASIR but it also involves modeling of system optics. This is unlike ASIR, which uses an idealized set of system optics

(as does FBP), resulting in similar data use per image. Model-based iterative reconstruction analyzes the x-ray beam at the focal spot, then analyzes the x-ray beam as it passes through the patient's body, and, again, analyzes the x-ray beam as it strikes the detector. The algorithm weighs each data point so that noisy projections have less influence on the final results, and this allows more accurate image reconstruction. Phantom experiments have shown that MBIR has the potential to further reduce image noise, improve spatial resolution, and thereby allow further dose reduction without compromising image quality.[25,26] With the incorporation of system optics information and therefore a more accurate account of voxel and focal spot size and geometry, one can expect improvements in spatial resolution.[25,26] Because MBIR is a complicated algorithm, using multiple iterations and multiple models, the reconstruction time is significantly longer than FBP and the other IR techniques are, even with dedicated state-of-the-art parallel processors. The reconstruction time in the present study was approximately 1 hour per case, although the exact time was not recorded because it was not a feature of the application software.

Vol.2, No.4, 93-98 (2013)
http://dx.doi.org/10.4236/ojrm.2013.24013

Open Journal of Regenerative Medicine

Evaluation of *in vivo* migration of chondrocytes from tissue-engineered cartilage that was subcutaneously transplanted in mouse model

Mariko Matsuyama[1,2], Yuko Fujihara[2,3], Ryoko Inaki[1], Satoru Nishizawa[4], Satoru Nagata[5], Tsuyoshi Takato[1,3], Kazuto Hoshi[1,2,3*]

[1]Department of Sensory and Motor System Medicine, The University of Tokyo Hospital, Tokyo, Japan;
*Corresponding Author: pochi-tky@umin.net
[2]Department of Cartilage & Bone Regeneration (Fujisoft), Graduate School of Medicine, The University of Tokyo, Tokyo, Japan
[3]Division of Tissue Engineering, The University of Tokyo Hospital, Tokyo, Japan
[4]Translational Research Center, The University of Tokyo Hospital, Tokyo, Japan
[5]NAGATA Microtia and Reconstructive Plastic Surgery Clinic, Toda, Saitama, Japan

Received 20 August 2013; revised 20 September 2013; accepted 2 October 2013

ABSTRACT

For regenerative medicine, clarification of *in vivo* migration of transplanted cells is an important task to secure the safety of transplanted tissue. We had prepared tissue-engineered cartilage consisting of cultured chondrocytes with collagen hydrogel and a biodegradable porous polymer, and we clinically applied it for treatment of craniofacial anomaly. To verify the safety of this tissue-engineered cartilage, we had syngenically transplanted the tissue-engineered cartilage using chondrocytes harvested from EGFP-transgenic mice into subcutaneous pocket of wild type mice, and investigated localizations of transplanted chondrocytes in various organs including cerebrum, lung, liver, spleen, kidney, auricle, gastrocnemius, and femur. After 8 to 24 weeks of the transplantation, accumulation of cartilaginous matrices was observed in tissue-engineered cartilage, while EGFP-positive transplanted chondrocytes were localized in this area. Otherwise, no EGFP was immunohistochemically detected in each organ, suggesting that subcutaneously-transplanted chondrocytes do not migrate to other organs through the circulation. In cartilage tissue engineering using cultured chondrocytes, risk for migration and circulation of transplanted cells seemed negligible, and that ectopic growth of the cells was unlikely to occur, showing that this is safe technique with regard to the *in vivo* migration of transplanted cells.

Keywords: Cartilage; Tissue Engineering; Chondrocyte; Migration

1. INTRODUCTION

Autologous chondrocyte transplantation has been attracting attention as a treatment of defects and injuries of cartilage tissue, which has poor self-repairing capability [1]. Tissue-engineered cartilage with various properties, such as that prepared by injection of cultured chondrocyte suspension [1] and that gelled by mixing with hydrogel [2]. We developed tissue-engineered cartilage by adding autologous cultured chondrocytes to a porous scaffold made of a biodegradable polymer, poly-L-lactic acid (PLLA) [3], in which collagen hydrogel was used as a mucilage to retain cells within the scaffold [4]. Since this regenerative cartilage tissue has firm hardness and a 3D structure, it is applicable for patients with cartilage deformations and defects associated with craniofacial diseases and traumas. We are using this three-dimensionally tissue-engineered cartilage to treat nasal deformation in a congenital craniofacial anomaly, cleft lip and palate. Since this is a novel clinical technique, its safety should be fully investigated [3].

In the guidelines for safety of medical devices using cultured cells established by the Japanese government, the evaluation of *in vivo* migration of transplanted cells is included as a safety item. Since it has been reported that bone marrow mesenchymal stem cells, from which chondrocytes are originated, transfer into the circulation after

transplantation and engraft various organs other than bone marrow [5], the possibility for cultured chondrocytes to enter the circulation or to migrate to other organs cannot be ruled out. Thus, we performed this study to investigate the *in vivo* migration of cultured chondrocytes after transplantation, and to ensure its safety.

In our previous study, the tissue-engineered cartilage matured 8 weeks after transplantation [6]. At 8 weeks, the transplanted chondrocytes were completely embedded within cartilaginous matrices, which implied that migration of chondrocytes from the transplants to other organs hardly occurred after that time. Thus, we investigated whether transplanted auricular chondrocytes were migrated to other organs by 8 weeks after transplantation. In addition, we examined it also at 24 weeks to confirm long-term safety.

2. MATERIALS AND METHODS

Firstly, we collected auricular cartilage from the ears of EGFP-transgenic mice (6-week-old males, n = 3, Experimental Animal Division RIKEN BioResource Center, Ibaraki, Japan). After sacrifice by anesthesia with somnopentyl at a fatal dose, approximately 15-mm longitudinal incision was made in the parietal skin. The skin was entirely dissected from the incision line to the apex of the auricle. The auricular cartilage tissue was cut immediately before the tympanum and shaken in 0.15% collagenase solution at 37˚C for 8 hours [7]. The isolated auricular chondrocytes were seeded at 500,000 cells/well in a 6-well plastic plate and cultured in 2 mL of DMEM containing 5% fetal bovine serum, 5 μg/mL insulin, and 100 ng/mL fibroblast growth factor (FGF)-2 [8] as the primary culture. Approximately 1 × 108 cells were recovered after 2 passages (P2). These 1 × 108 cells and 1 mL of 1% collagen hydrogel (atelocollagen, Koken, Tokyo, Japan) were mixed on ice for about 10 minutes. The mixture was infiltrated into sterile PLLA porous scaffold (5 × 5 × 3 mm, KRI, Kyoto, Japan), and gelled in the dish at 37˚C for 2 hours to avoid drying (**Figure 1, 0 wk**).

The tissue-engineered cartilage composed of the PLLA/gel/cells (n = 3) was transplanted under the dorsal skin in C57BL/6 mice (Nippon Bio-Supp. Center, Tokyo, Japan) under anesthesia with 16 μL/animal of somnopentyl (**Figure 1, 0 wk**). The transplants and eight kinds of target organs (cerebrum, lung, liver, spleen, kidney, auricle, gastrocnemius, and femur) were excised after 8 and 24 weeks, fixed in 4% paraformaldehyde for one hour, immersed in PBS, and embedded in paraffin. The serial sections with a 5-μm thickness were then prepared.

After observation under excitation fluorescence, the sections of samples were subjected to toluidine blue staining, hematoxylin and eosin staining, and immunostaining of EGFP. To detect transplant-derived cells, non-serial 10 sections were selected from each organ [9], deparaffinize with xylene, hydrated with stepwise dilutions of ethanol, immersed in PBS, and subjected to immunostaining of EGFP. To activate antigen, the sections were placed in a mixture of 15 mL of Dako Real Target Retrieval Solution (×10) (Dako, Tokyo, Japan) and 135 mL of 98˚C hot water, boiled for 15 minutes, kept standing at room temperature for 15 minutes, and immersed in PBS for 5 minutes. This procedure was performed twice. For blocking, 10% normal goat serum was dripped on the sections and left standing at room temperature for 10 minutes. After removing moisture, the primary antibody, Invitrogen anti-green fluorescent protein rabbit IgG fraction (anti-GFP IgG) (Life Technologies Corporation, Carlsbad, CA, USA), was dripped on the sections (1:1000) and incubated at 37˚C for 90 minutes. For the control, normal rabbit IgG (SANTA CRUZ BIO- TECHNOLOGY, INC.) was used instead of the primary antibody. After immersing in PBS for 5 minutes twice, the secondary antibody, Anti-IgG, rabbit, goat-poly, Bio- tin (Vector Laboratories, Burlingame, CA, USA), was dripped on the sections (1:200) and left standing at room temperature for 30 minutes. After immersing in PBS for 5 minutes twice, vectastain ABC (Vector Laboratories, Burlingame, CA, USA) was dripped on the sections and left standing at room temperature for 30 minutes (ABC reaction). After immersing in PBS for 5 minutes twice, the sections were reacted with substrate DAB, and immersed in Milli-Q water. For counter staining, hematoxylin was used. The sections were then dehydrated and sealed.

The organs were similarly collected from 6-week-old

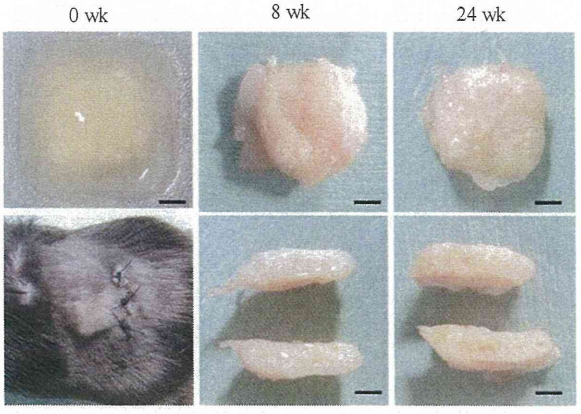

Figure 1. Macroscopic findings of tissue-engineered cartlage. Tisue-engineered cartilage comprised of PLLA scaffold with the mixture of green mouse auricular chondrocytes and atelocollagen was prepared (left top) subcutaneously transplanted into the dorsal region of C57BL/6 mice (left bottom). Whole (top) and half cross-section (bottom) of the transplants, 8 and 24 weeks after transplantation. Scale bar: 1 mm.

EGFP-transgenic mice (positive control) and 57BL/6 mice (negative control) and subjected to immunostaining of EGFP. The organ was judged as EGFP-positive when an EGFP-positive cell was present in one or more of the 10 sections [9].

3. RESULTS

The tissue-engineered cartilage removed 8 and 24 weeks after transplantation consisted in elastic soft tissue (**Figure 1, 8 and 24 wks**). The excised transplants were evaluated histologically and immunohistochemically. In toluidine blue staining, metachromasia was noted throughout the transplants at 8 and 24 weeks, suggesting the maturation of regenerative cartilage.

A large area in the transplants was occupied by regenerative cartilage at both 8 and 24 weeks, while the rate was almost similar between them (**Figures 2 (a)** and **(b)**). Under 490-nm excitation fluorescence, green fluorescence was noted in the cartilaginous region (**Figure 2**(c)). In immunohistochemical staining of EGFP, EGFP-positive cells were corresponding to chondrocytes in the cartilaginous region (**Figure 2**(d)). These findings suggested that chondrocytes in the regenerative cartilage were derived from the cells of the transplants.

The eight target organs were also excised when the transplant was removed at 8 or 24 weeks, and subjected to immunohistochemical staining of EGFP. In theEGFP-transgenic mice, EGFP-positive cells were present in all these organs (**Figures 3** and **4**, **EGFP**). In the C57BL/6 mice, no positive cells were noted in any of the eight organs (**Figures 3** and **4**, **before transplantation**). At 8 and 24 weeks after transplantation, no EGFP-positive cells were noted in any of the eight organs (**Figures 3** and **4**, **8 and 4 wks**).

The number of positive cells was 0 in any of the eight organs at 8 or 24 weeks after transplantation, showing that chondrocytes in the transplants did not migrate to other organs (**Table 1**).

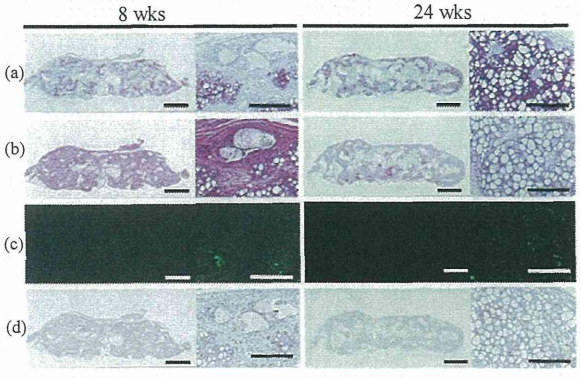

Figure 2. Histological analyses of tissue-engineered cartilage. (a) Toluidine blue staining of tissue-engineered cartilage. Abundant metachromasia was noted 8 and 24 weeks after transplantation, while cartilaginous tissue was extensively observed. (b) Hematoxylin and eosin staining of tissue-engineered cartilage, 8 and 24 weeks after transplantation. Maturation of tissue-engineered cartilage was observed at both weeks. (c) Localization of EGFP-positive chondrocytes was detected under 490-nm excitation fluorescence. (d) Immunohisto- chemical staining of EGFP in tissue-engineered cartilage. The cartilagenous region was constructed only with EGFP-positive transplanted chondrocytes, being consistent with the localization of EGFP-positive cells in C. Scale bar: 1 mm (low magnification) and 100 μm (high magnification).

4. DISCUSSION

We transplanted tissue-engineered cartilage containing EGFP-positive auricular chondrocytes into mice, and histologically confirmed that no chondrocytes migrated to the other organs 8 and 24 weeks after transplantation. As a phenomenon of cell migration between organs, me-

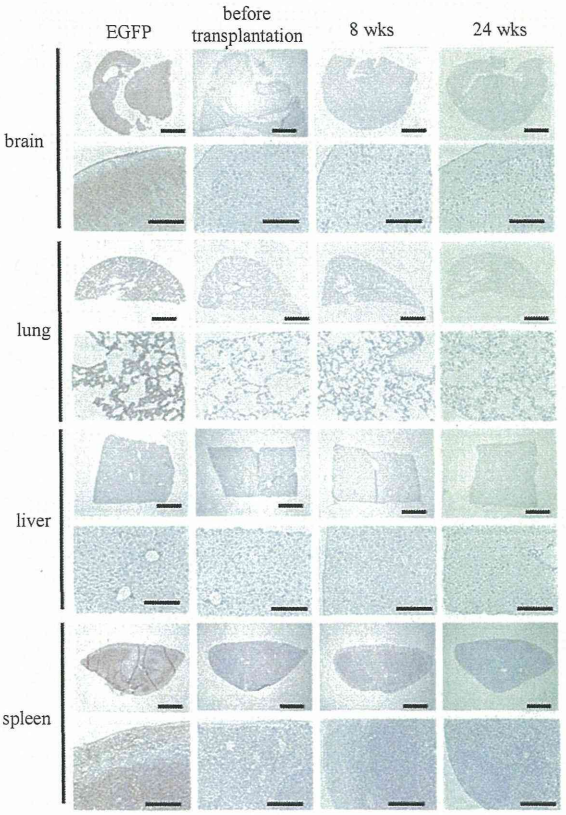

Figure 3. Localization of transplanted chondrocytes in cerebrum, lung, liver, and spleen. Typical photographs of immunohistochemical staining of EGFP in cerebrum, lung, liver, and spleen of C57BL/6 mice were shown before transplantation or at 8 and 24 weeks after transplantation. No EGFP-positive cells were noted in any of the organs. In green mice as the positive control, EGFP-positive cells were noted in all of the organs (EGFP). Staining was performed in 3 animals, and similar results were obtained in all. Scale bar: 1 mm (low magnification) and 100 μm (high magnification).

